processes

MDPI

Article

Research on Wave Velocity Disparity Characteristics between Impact and Outburst Coal Seams and Tomography of Hazardous Zones

Zhixin Fang [1], Qiang Liu [2], Liming Qiu [2,3,*], Zhanbiao Yang [3,4], Zhaohui Cao [2], Guifeng Wang [5], Zehua Niu [3,4] and Yingjie Zhao [2]

[1] School of Engineering, Newcastle University, Newcastle upon Tyne NE1 7RU, UK
[2] School of Civil and Resource Engineering, University of Science and Technology Beijing, Beijing 100083, China
[3] State Key Laboratory of Coking Coal Resources Green Exploitation, Pingdingshan 467002, China
[4] China Pingmei Shenma Holdings Group Co., Ltd., Pingdingshan 467000, China
[5] School of Mines, China University of Mining and Technology, Xuzhou 221116, China; wgfskl@163.com
* Correspondence: qiulm@ustb.edu.cn

Abstract: To investigate the variations in wave velocity fields between impact and outburst coal seams, we analyzed the fluctuations in wave velocity under loading conditions for both coal types. A comprehensive methodology was developed to correct coal wave velocities in response to stress and gas presence, which was then applied to field assessments of hazardous regions. Our findings reveal significant differences in wave velocity alterations between impact and outburst coal seams during loading-induced failure. Gas pressure exhibits a negative correlation with wave velocity in outburst coal (correlation coefficient $R^2 = 0.86$), whereas wave velocity in impact coal demonstrates a positive correlation with stress ($R^2 = 0.63$). A robust methodology for correcting coal wave velocities in response to stress and gas presence was established to enable more accurate measurement of wave velocity changes. In field applications, seismic wave computed tomography identified stress anomalies that closelycorresponded with geological structures and mining operations, effectively pinpointing hazardous zones. The abnormal wave velocity coefficient ranges for outburst coal seams and impact coal seams are −0.6 to 0.25 and −0.35 to 0.16, respectively, which correspond well with the field stress distribution.

Keywords: rock burst; coal and gas outburst; wave velocity field; tomography

Citation: Fang, Z.; Liu, Q.; Qiu, L.; Yang, Z.; Cao, Z.; Wang, G.; Niu, Z.; Zhao, Y. Research on Wave Velocity Disparity Characteristics between Impact and Outburst Coal Seams and Tomography of Hazardous Zones. *Processes* **2024**, *12*, 1558. https://doi.org/10.3390/pr12081558

Academic Editor: Yuanyuan Pu

Received: 13 June 2024
Revised: 16 July 2024
Accepted: 18 July 2024
Published: 25 July 2024

1. Introduction

The severity of coal-rock dynamic disasters has intensified with the increasing depth and intensity of coal mining [1]. These incidents are sudden occurrences resulting from the dynamic progression of coal-rock deformation and fracture induced by mining activities [2,3]. Effective monitoring and timely issuance of warnings for these phenomena are paramount for disaster mitigation. The comparative analysis of wave velocity variations across various coal and rock dynamic disasters, alongside the identification of hazardous zones, represents pressing scientific inquiries that demand attention.

Diverse monitoring methodologies have been developed and applied, predicated on distinct disaster occurrence mechanisms and their resultant physical manifestations, yielding promising outcomes [4]. In the process of coal failure, acoustic signals are generated [5]. Acoustic signal characteristics are used to study rock mechanical properties [6] and reveal the spatial-temporal effect of rock damage [7,8], leading to the widespread adoption of microseismic technology for rock burst monitoring [9,10]. He et al. [11] observed that coal-rock failure emits electromagnetic radiation signals, exploitable for early warning [12] and positional analysis of dynamic disasters [13]. Seismic wave computed tomography (CT), an innovative geophysical technique, finds utility in geological exploration [14], stress distribution detection [15], and other domains. Dou et al. [16] established technical indicators for seismic wave CT detection and shock hazard evaluation, including the wave

velocity anomaly coefficient (A_n) and the gradient change coefficient of wave velocity (V_G), demonstrating the technology's dynamic evaluation and prediction capabilities for shock hazards. Wang et al. [17] utilized time-lapse seismic tomography to identify activity-affected areas and stress concentrations in mines. Ma et al. [18] analyzed three-dimensional passive microseismic signals of seismic activity at the Sudbury Creton mine in Ontario, Canada, and developed a wave velocity field model, confirming the presence of high wave velocity anomalies in high-stress areas. Zhao et al. [19] established a method for analyzing the relative permeability of coal seams based on the correlation between wave velocity, stress, and permeability, and conducted practical on-site experiments. Khayer K inferred the permeability and saturation of rock formations by analyzing the propagation characteristics of acoustic waves [20,21]. Hu et al. [15] used active velocity tomography technology to assess the stress status and rock burst risk in deep coal mines, establishing the relationship between wave velocity and formation stress, and found that the mining energy release area corresponds with the high-speed seismic field.

Previous research has predominantly focused on utilizing seismic wave CT technology for monitoring and predicting rock bursts [15,16,22]. However, there remains a paucity of investigations into microseismic monitoring and wave velocity field analysis specific to outburst mines. Peng et al. [23] conducted microseismic monitoring during the hydraulic fracturing process in gas mines, revealing that alterations in coal seam fractures can induce changes in the wave velocity field, consistent with findings from the direct current method. In contrast to rock burst mines, outburst coal exhibits diminished structural integrity [24] and elevated gas content. Furthermore, gas exerts a detrimental impact on wave velocity [19]. Consequently, the presence of gas reduces coal stress, thereby altering porosity and leading to anomalous wave velocity distributions.

An analysis was undertaken to discern disparities in wave velocity alterations between rock burst mines and outburst mines, delineating the unique wave velocity fields characteristic of these dynamic disasters. On-site hazardous zones were classified utilizing seismic wave computed tomography (CT). This study empirically explores the influence of gas on outburst coal and the concomitant changes in wave velocity during coal impact failure. Subsequently, a comprehensive method for determining the elastic wave velocity in coal, which is affected by the presence of gas and static stresses. Leveraging the corrected wave velocity field, a comparative analysis was conducted on the characteristics of rock burst and coal and gas outburst danger areas. The comprehensive flowchart of the research is shown in Figure 1.

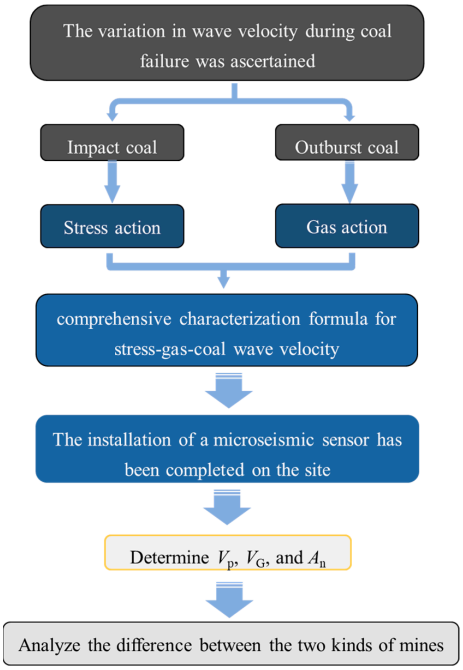

Figure 1. Flowchart.

2. Methodology

2.1. Experiment System

(1) Loading system

In this experiment, the MTS815 electro-hydraulic servo rock mechanics testing system was used. The main equipment is shown in Figure 2. The MTS815, produced by MTS Systems Corporation, Minnesota, USA, is a hydraulic servo mechanical system. It applies confining pressure to the sample through hydraulic oil and axial pressure through the upper and lower axial pressure heads. The system includes a pneumatic feeding mechanism that can test the mechanical and permeability characteristics of various coal and rock materials under complex stress conditions and perform loading tests on gas-containing coal and rock.

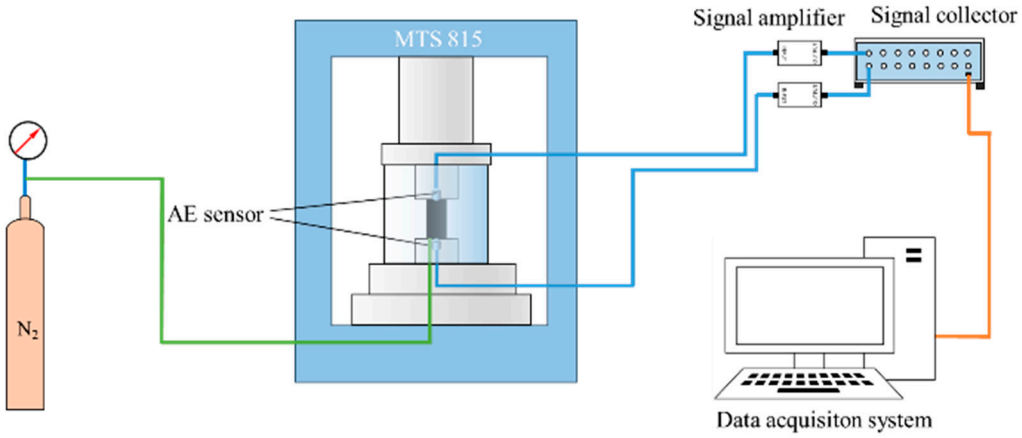

Figure 2. Experiment system.

(2) Acoustic emission probe layout

The data acquisition and processing device for acoustic emission signals adopts the the DS5 series full-information acoustic emission signal analysis system produced by Ruike Instrument Technology Co., Ltd., Guangzhou, China, which mainly consists of DS5 acoustic emission tester, sensors, amplifiers, etc. In this experiment, two probes were arranged in the vertical direction; the upper probe excites waveform signals, while the bottom probe receives signals. The external acoustic emission signal amplifier of the probe has the same amplification factor. The waveform of all acoustic emission events during the dynamic loading process of coal-rock samples was collected, resulting in the full waveform diagram of the acoustic emission signal during the dynamic loading process of coal-rock. After collecting the acoustic emission waveform, the standard wave was used to identify the excitation point and initial arrival point of the wave, determine the time required for the wave to pass through the coal sample, and then calculate the longitudinal wave velocity based on the length of the coal sample. The arrangement of wave probes is shown in Figure 1.

2.2. Sample Preparation

The raw coal for the outburst coal-rock sample used in the experiment was extracted from the No. 22 coal seam of the Jinjia coal mine, a typical outburst mine in the Panjiang mining area, China. Due to the soft-coal quality in the Jinjia mine's outburst coal seam, it is not possible to obtain a complete raw coal sample through drilling. Therefore, the coal samples used in this study were cylindrical specimens, each with a diameter of 50 mm and a height of 50 mm, with an end-face non-parallelism not exceeding 0.05 mm, compressed from coal powder. The raw coal sample for the impact test was selected from the Xinzhouyao Coal Mine. After on-site sampling, it was sent to the laboratory and prepared as a cylindrical sample with a diameter of 50 mm and a height of 100 mm. The basic parameter information of each sample is shown in Table 1.

Table 1. Original parameters of the sample.

Sample Number	Diameter/mm	Height/mm	Weight/mm
#1	51.16	53.32	145.14
#2	50.94	50.06	140.64
#3	49.84	100.02	264.34
#4	49.83	100.07	264.37

2.3. Experiment Project

The gas pressure injection process affects the wave velocity test as follows: For Sample #1, the axial pressure was initially increased to 12 MPa, followed by the immediate introduction of 0.5 MPa of gas. Acoustic emission waveform collection began immediately thereafter. The gas pressure was then increased to 1 MPa and subsequently to 3 MPa, with waveform data collected every 10 s. For Sample #2, the same method was applied as for Sample #1, but with gas pressures of 1, 2, 3, 4, and 5 MPa, and waveform data were similarly collected every 10 s.

Measurement of the uniaxial compression wave velocity of outburst coal included the following: Uniaxial compression tests on outburst coal with an axial compression loading rate of 15 N/s and longitudinal wave velocity measurements every 3 s. The test concludes when the fracture percentage reaches 70%.

2.4. Waveform Testing Methods

To ensure the accuracy of test results, a preload of 500 N is applied to the specimen before the test to eliminate any gaps between the loading device and the specimen. The pulse width for automatic acquisition is set to 20 μs, and the pulse period is set to 2000 μs. The file is saved once the pulse period ends.

Figure 3 presents a schematic diagram of the standard wave principle for longitudinal waves [25]. The waveforms received by different probes are recorded on separate channels, as illustrated in the figure. Mark the position of the probe receiving the longitudinal wave, and then identify the corresponding time node to calculate the propagation time required for the wave to travel a length L during the loading process.

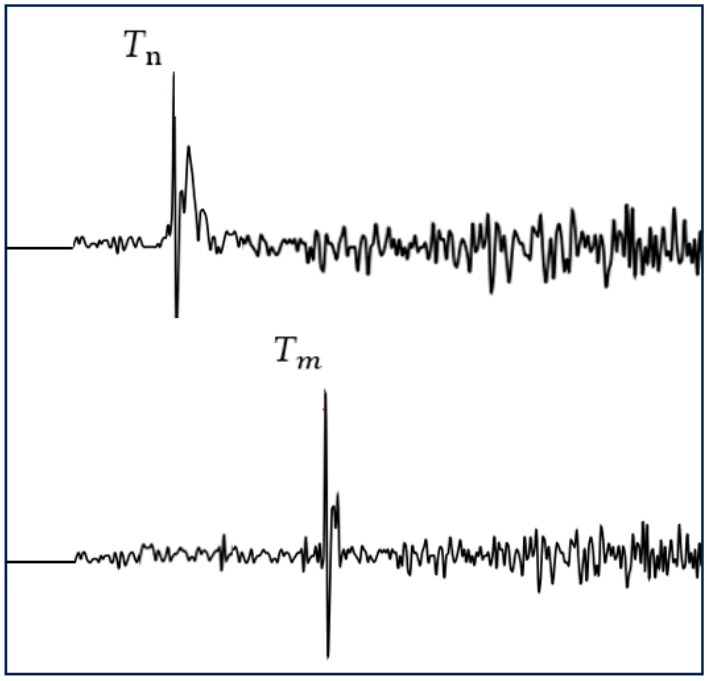

Figure 3. Schematic diagram of wave speed testing.

The coal sample is calculated using Equation (1) for inflation or wave velocity, where $T_m - T_n$ is the propagation time of the sample through a length of $L(1 - \varepsilon)$ during the loading process, and ε is the axial strain.

$$V_p = \frac{L(1-\varepsilon)}{T_m - T_n} \quad (1)$$

where: V_p—longitudinal wave velocity, m/s; T_m—the time when longitudinal waves start to propagate; T_n—the time when the receiving probe receives the longitudinal wave; and L—the height of the sample before loading.

3. Results

3.1. Analysis of Changes in Wave Velocity and Gas Influence during Coal Body Failure under Load

The variation in coal wave velocity under different gas pressures is shown in Figure 4. It can be observed that as the gas pressure increases, the wave velocity of the #1 and #2 coal samples continuously decreases. The wave velocity of the #1 sample decreased by 13.66% as the gas pressure increased from 0.5 MPa to 3 MPa. The wave velocity of the #2 sample decreased by 38.26% as the gas pressure increased from 0.5 MPa to 5 MPa. Data fitting revealed that both have a decreasing slope of 46.77, which is essentially the same. During the process of gas adsorption in coal, micropores are affected by gas degradation and transform into larger pores, resulting in a relative increase in porosity [26]. Studies have shown that changes in porosity alter the material structure of coal, leading to changes in wave velocity [27]. Therefore, the increase in gas pressure causes damage and expansion of coal pores, weakens their mechanical properties, and thus reduces the wave velocity of coal [28].

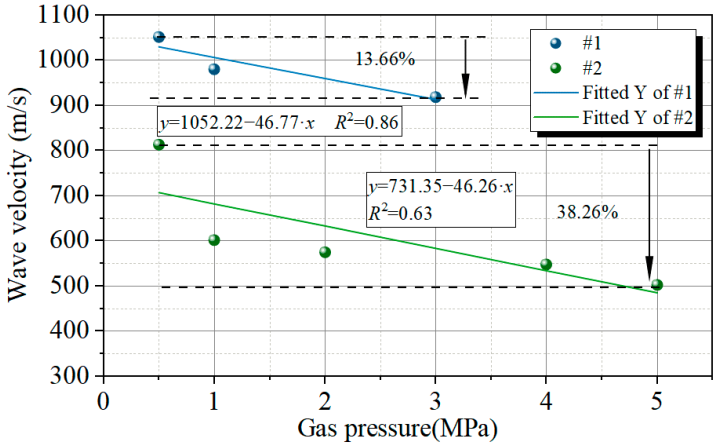

Figure 4. The variation law of outburst coal wave velocity with gas pressure.

For impact coal, the variation of wave velocity with stress is illustrated in Figure 5. It can be observed that with the increase in stress, the wave velocity of the #3 and #4 coal samples continues to increase. As the stress on the coal increases until failure occurs, the wave velocity of the #3 coal sample increases by 47.23%, and the #4 coal sample increases by 52%. With the increase in stress, the internal pores of the coal body are compressed and reduced, the internal joints are closed, and the wave velocity increases accordingly. Zhao et al. [19] found that the change in wave velocity of gas-containing coal is determined by the negative effect caused by gas adsorption and the compression of the matrix. Therefore, for rock burst mines, when conducting microseismic analysis, only the influence of stress concentration and the properties of coal-rock need to be considered. For outburst mines, a more comprehensive consideration is needed to account for the effects of gas and stress on coal wave velocity.

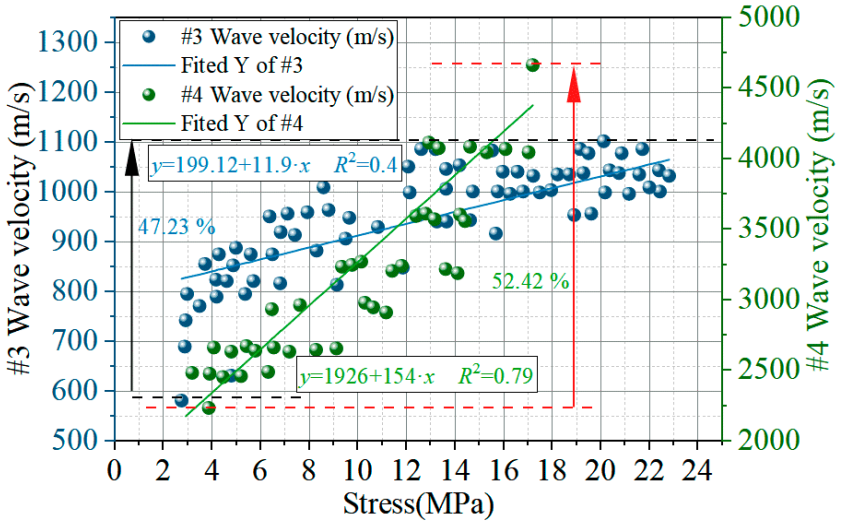

Figure 5. The variation law of shock coal wave velocity with stress.

3.2. Comprehensive Stress Gas Coal Wave Velocity Characterization Method

The above experimental results indicate that changes in coal gas pressure and stress significantly affect its wave velocity variation. The gas pressure in most coal seams in China does not exceed 2 MPa. As shown in Figure 3, the range of stress changes' impact on coal wave velocity is around 15%. The impact range of stress changes on coal wave velocity is around 50%. Thus, although the influence of gas is smaller than that of stress, it cannot be ignored.

From the fitting results of the experimental data in Figure 3, the wave velocity demonstrates a linear relationship with the decrease in gas pressure. For the same type of coal sample, the slope remains essentially consistent. Assuming the slope represents the coefficient of influence on coal wave velocity, the relationship between gas pressure and coal wave velocity is as follows:

$$V_{p0} = V_0 + k \cdot P_g \tag{2}$$

where V_0 represents the wave velocity of the initial gas pressure of 0 MPa, m/s; V_{p0} is the wave velocity of the initial gas pressure of P_g MPa, m/s; k is the coefficient of influence of gas on the wave velocity of coal, m/(s Pa); and P_g is the gas pressure, Pa.

From the influence of stress changes on wave velocity, it is observed that as stress increases, the wave velocity approximately doubles. This trend aligns with previous experimental results [19,22]. Assuming a linear trend in the analysis process, we fit the data accordingly, as illustrated in Figure 5. The relationship between shock coal wave velocity and stress is further defined as follows:

$$V_{p1} = V_{p0} + k_1 \cdot V_{p0} \cdot P_p \tag{3}$$

where V_{p0} represents the wave velocity at an initial stress of 0 MPa (m/s); V_{p1} represents the wave velocity at an initial stress of P_p MPa, m/s; k_1 denotes the coefficient of influence of gas on the wave velocity of coal, 1/Pa; and P_g is the gas pressure, Pa.

Although the above research analyzed the wave velocity properties of coal samples from both rock burst mines and outburst mines, the focus was on analyzing the influence of gas action on the wave velocity of the coal body in outburst coal samples. In rock burst mines, the effect of gas can be ignored. In outburst mines, the coal body is jointly affected by gas and stress fields. As gas pressure increases, coal damage gradually intensifies, leading to instability in its properties [29].

In rock burst mines, the accumulation and sudden release of impact energy are the fundamental causes of disasters [30–32]. Therefore, despite the differences in properties between impact coal and outburst coal, the influence on wave velocity has an inherent

unity. Furthermore, considering Formulas (2) and (3), a comprehensive characterization formula for stress–gas coal wave velocity was derived.

$$V_p = V_0 + k \cdot P_g + k_1 \cdot V_0 \cdot P_p \tag{4}$$

In the above equation, we analyzed the variation in the ideal coal wave velocity. According to this experiment, k is assigned as -0.046 m/(s Pa) and k_1 is assigned as 0.00013 1/Pa. In fact, the wave velocity during the coal body failure process exhibits a certain degree of fluctuation. However, the stress and displacement within the coal body are non-uniform, leading to different variations in wave velocity in different regions. Assuming an initial wave velocity of 1000 m/s, as shown in Figure 6, the variation of coal wave velocity under comprehensive stress gas conditions is illustrated. The dual influence of stress and gas pressure leads to variation in wave velocity. For rock burst mines, Figure 6 depicts a special case where P_g = 0 MPa, which belongs to the one-dimensional case of a two-dimensional problem. For outburst mines, the wave speed is influenced by both factors. The stress field and gas field of coal seams are relatively complex; therefore, the study of outburst mines presents greater complexity.

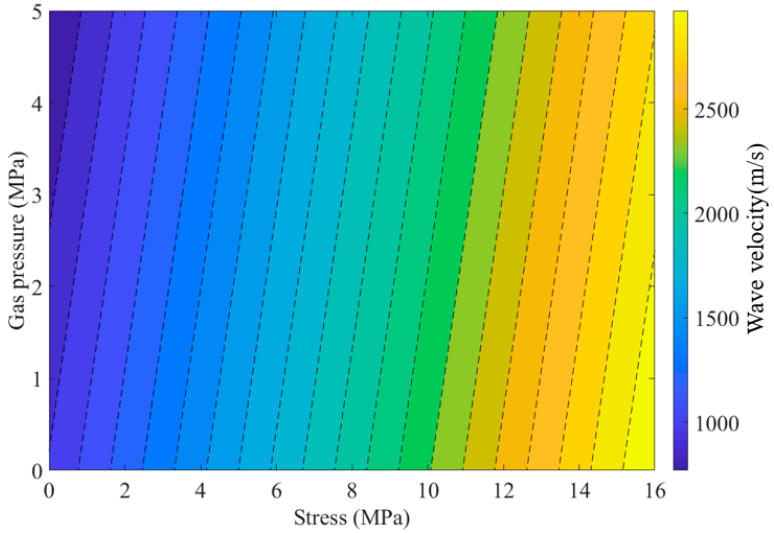

Figure 6. Comprehensive stress–gas coal body wave velocity changes.

3.3. Principle of Stress Field Detection by Vibration Wave CT

The Shockwave CT technology is achieved via waveform inversion for imaging purposes. The system primarily comprises a series of signal collectors and detectors, as shown in Figure 7. The velocity distribution, V (x, y, z), or slowness, S (x, y, z) = $1/v$ (x, y, z), is inverted based on the initial travel time data of the received seismic wave. Assuming the propagation path of the i-th seismic wave is L_i and its travel time is T_i, then the following is formulas are used:

$$V = \frac{L}{T} \rightarrow V \cdot T = L \tag{5}$$

$$T_i = \int_{L_i} \frac{ds}{V(x,y,z)} = \int_{L_i} S(x,y,z)ds \tag{6}$$

$$T_i = \sum_{j=1}^{M} d_{ij} S_j \tag{7}$$

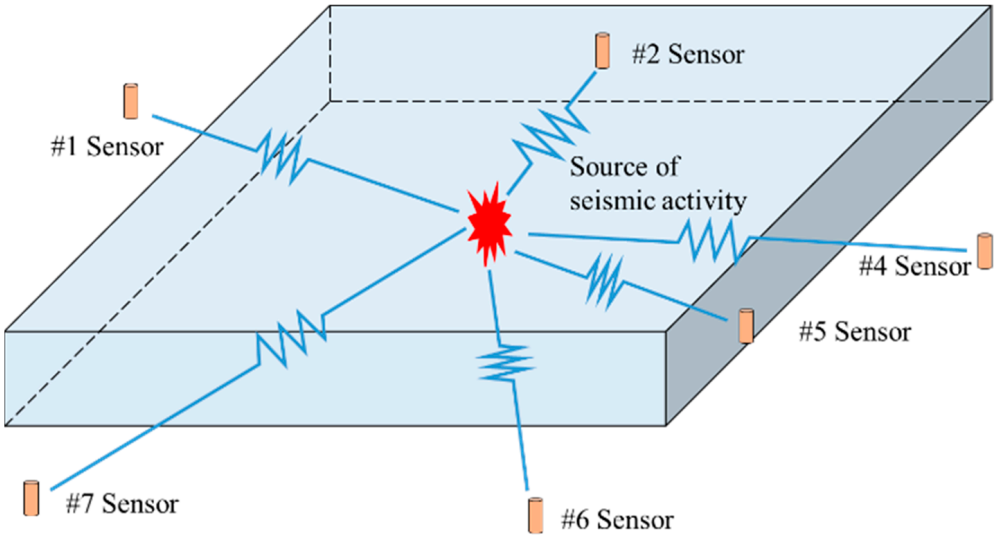

Figure 7. Schematic diagram of detection principle.

Here, d_{ij} represents the length of the i-th seismic wave ray passing through the j-th grid; N represents the total number of rays; and M represents the number of grids.

When a large number of rays (such as M rays) pass through the inversion region, according to Formula (7), M equations (i = 1,2, …, M) can be obtained for the unknown quantity S_j (J = 1,2, …, N). The M equations are combined to form a linear system of equations from Equation (9):

$$\begin{cases} T_1 = a_{11}S_1 + a_{12}S_2 + a_{13}S_3 + \cdots + a_{1j}S_j \\ T_2 = a_{21}S_1 + a_{22}S_2 + a_{23}S_3 + \cdots + a_{2j}S_j \\ \cdots \quad \cdots \\ T_i = a_{i1}S_1 + a_{i2}S_2 + a_{i3}S_3 + \cdots + a_{ij}S_j \end{cases} \tag{8}$$

Written in matrix form, Equation (9) is as follows:

$$AS = T \tag{9}$$

where: $A = (a_{ij})_{M\times N}$—distance matrix; $T = (T_i)_{M\times 1}$—travel time vector, i.e., the first arrival travel time obtained by the receiver; and $S = (S_i)_{N\times 1}$—slowness column vector.

Furthermore, Dou et al. [16,33] proposed the following anomaly coefficient A_n of coal seam seismic wave velocity based on the degree of stress concentration and abnormal changes in different areas of coal-rock layers:

$$A_n = \frac{V_p - V_p^a}{V_p^a} \tag{10}$$

In the formula, V_p^a is the average value of the model wave velocity, m/s.

After considering Formulas (4) and (10) comprehensively, we obtain the following:

$$A_n = \frac{V_0 + k \cdot P_g + k_1 \cdot V_0 \cdot P_p}{V_0^a + k \cdot P_0^a + k_1 \cdot V_0^a \cdot P_p^a} - 1 \tag{11}$$

The superscript a in the formula represents the average value of this value

The index of abnormal gradient of wave velocity change utilizes the gradient value of wave velocity change to predict potentially dangerous areas. When there are geological structures such as folds, faults, and fractured zones in front of the excavation roadway, these structures affect the stress balance in the area, resulting in uneven stress distribution. From the experimental relationship between longitudinal wave velocity and stress, it

can be inferred that fracture zones correspond to low wave velocity zones, while stress concentration zones correspond to high wave velocity zones. Between these two zones is a transitional zone from high wave velocity to low wave velocity, characterized by a large gradient in wave velocity variation.

$$V_G(i,j) = V_p(i,j)Grad(i,j) \quad (12)$$

4. Geological Setting

4.1. Analysis of CT Hazardous Areas for Seismic Waves in Outburst Coal Seams

The prominent mine is situated within the Jinjia Coal Mine, located in the Panjiang mining area. The project is located at the 11,224 working face, situated in the second section of the 22# coal seam on the south wing of the Jinyi mining area shaft, above the 1721 level. The main tunnels in the 11,224 working face area include the 11,224 transportation roadway, the 11,224 cutting hole, and the 11,224 return airway. Seismic wave CT is monitored via the SOS microseismic monitoring system, and the arrangement scheme of microseismic probes is shown in Figure 8. In the figure, red dashed lines is the contour lines of gas pressure. Specifically, seismic sensors 1#, 2#, and 4# are arranged in the 11,224 return airway at distances of 170 m and 190 m, respectively. Seismic sensors 5# and 6# are arranged in the 211 transportation stone gate at a distance of 210 m. Seismic sensors 7# and 8# are arranged in the 11,224 excavation transportation roadway. There is a geological anomaly area about 20 m to the right of the 11,224 cut, characterized by fractured rock mass and a missing 22# coal seam. The layout of the probes has effectively surrounded the 11,224 working face, with the testing period being the head-on excavation period of the 11,224 transport roadway. Figure 9 illustrates the comparison between the upper and lower levels of the 11,224 working face. In the upper part of the entire 11,224 working face, there are two ridges from top right to bottom left and a valley between the two mountains, resulting in variations in the original stress distribution of the working face.

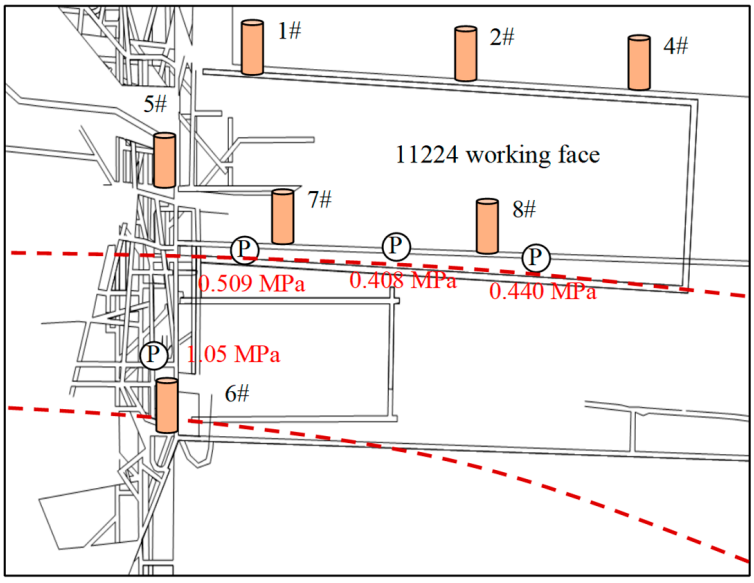

Figure 8. Position of working face and distribution of sensors.

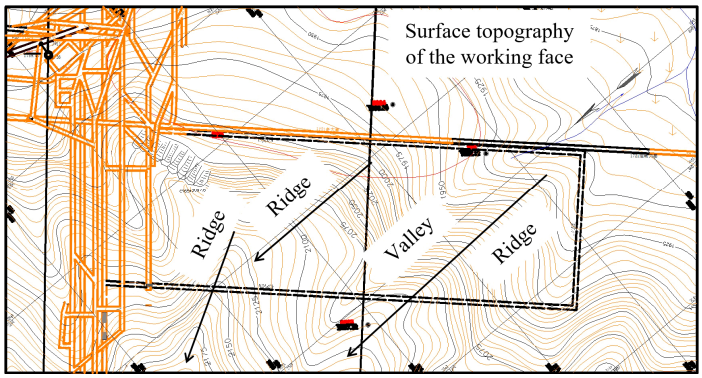

Figure 9. Comparison diagram of the upper and lower parts of the 11,224 working face well.

4.1.1. Comparison of V_p Correction before and after Wave Velocity Field in Gas Containing Coal Seams

Figure 10 illustrates the distribution of the wave velocity field in the 11,224 working face. The inversion results of wave velocity show a narrow band of increased stress, aligning with the position of surface valleys. After correcting the wave velocity field, a decrease in the high-stress area was observed, and the area greater than 6 km/s was significantly reduced. This indicates that there is a reduction in the wave velocity field after accounting for the effect of gas on wave velocity reduction. Meanwhile, considering that the gas distribution is between 0.5 and 1 MPa, the gas pressure and its variation gradient are relatively small, and their impact on wave velocity is minimal. Define high wave velocity as regions I and II, and regions with reduced wave velocity as region III.

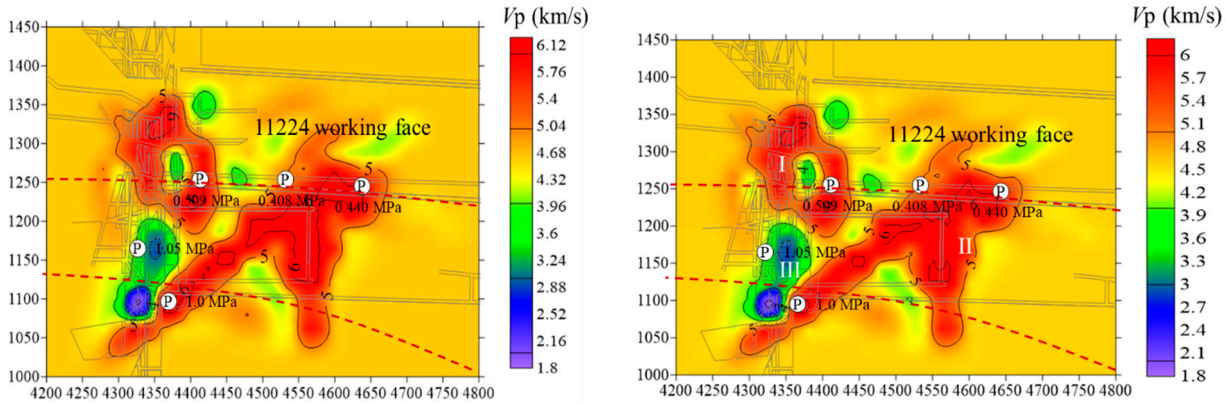

Figure 10. CT results of the original wave velocity field in the 11,224 working face. (**a**) Before correction; (**b**) Revised.

Overall, seismic wave CT is related to the stress field, gas field, and coal properties of coal seams [25]. These properties are also primary factors causing coal-rock dynamic disasters. The CT wave velocity field of seismic waves thus indicates the positioning results of areas with different mechanical properties of coal, which belongs to the same origin detection method as microseismic detection [17]. Consequently, the red area in the figure represents the high-stress area, while the blue area represents the stress unloading area. There are various possibilities for the stress unloading area; primarily, it is distributed around the roadway, which may be related to the development of cracks caused by mining activities [34]. However, this explanation is relatively weak for Region I. Another possibility is that both areas are stress concentration zones, but Region III has already ruptured due to the influence of the original stress, while Region I has received relatively little original stress, forming a high wave velocity region. This explanation can also be compared with the distribution of gas concentration, indicating that the gas

pressure in Region III is the highest, suggesting that its resolution is significantly greater than that of the other two regions.

4.1.2. Comparative Analysis of Abnormal Wave Velocity Values

Figure 11 illustrates the values of the wave velocity anomaly coefficient before and after correction. The distribution of wave velocity anomaly coefficients closely resembles that of wave velocity distribution; both exhibit a narrow and high-value area, corresponding to the strong danger level in Table 2. After correcting the original A_n values, as shown in Figure 11b, it was observed that post-correction, the area with A_n values between -0.25 and -0.075 merged, while the area with values less than -0.25 diminished. Additionally, a differential analysis was conducted on the data before and after correction, with the results presented in Figure 12. Figure 12 illustrates the differential results of the wave velocity anomaly coefficients before and after correction. The results indicated significant changes in the low A_n region, with high values reaching approximately 0.003, whereas changes in the high A_n region were about -0.0016, roughly half that of the low A_n region.

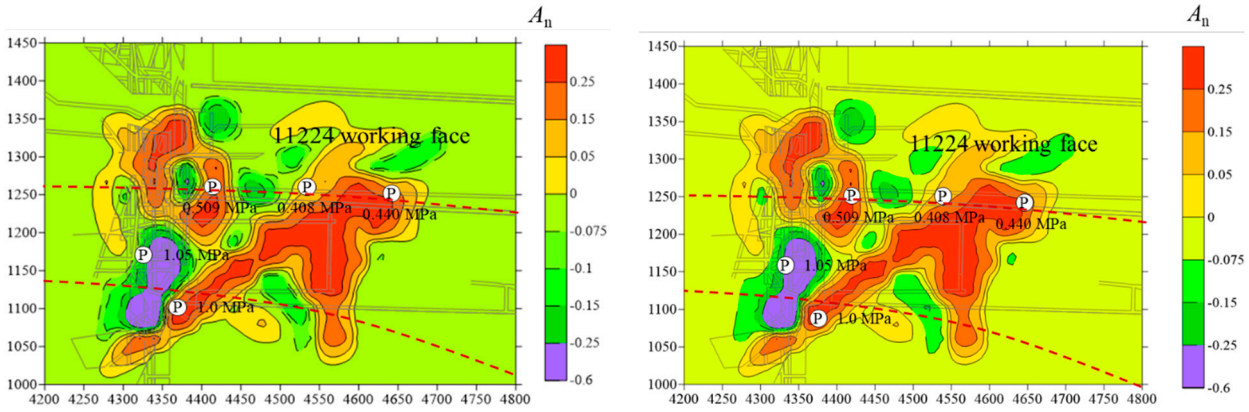

Figure 11. Abnormality coefficient A_n of original wave velocity in working face 11,224. (**a**) Before correction; (**b**) Revised.

Table 2. Corresponding relationship between positive and negative changes in wave velocity and degree of anomaly.

Anomaly Index	Risk Level	A_n/%
0	None	$-7.5 < A_n/A_n < 5$
1/−1	Weak	$-15 < A_n \leq -7.5/5 \leq A_n < 15$
2/−2	Middle	$-25 < A_n \leq -15/15 \leq A_n < 25$
3/−3	Strong	$A_n \leq -25/25 \leq A_n$

Figure 13 illustrates the corrected anomaly index of the wave velocity gradient change. The anomaly index of the wave velocity gradient reflects the rate of wave velocity change. Most gradient changes are relatively slow, with the primary areas in the graph changing around 0.05, whereas most of the corresponding anomalous wave velocity areas are less than 0.45. The highest value of the anomaly index for the gradient of wave velocity change is 1.05, which corresponds to the junction between the extremely low and peak values of wave velocity.

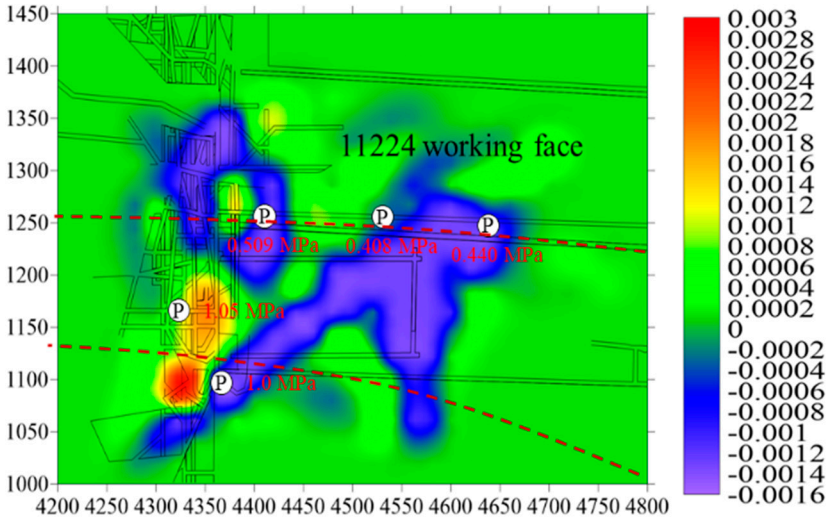

Figure 12. Differences in wave velocity anomaly coefficients before and after correction.

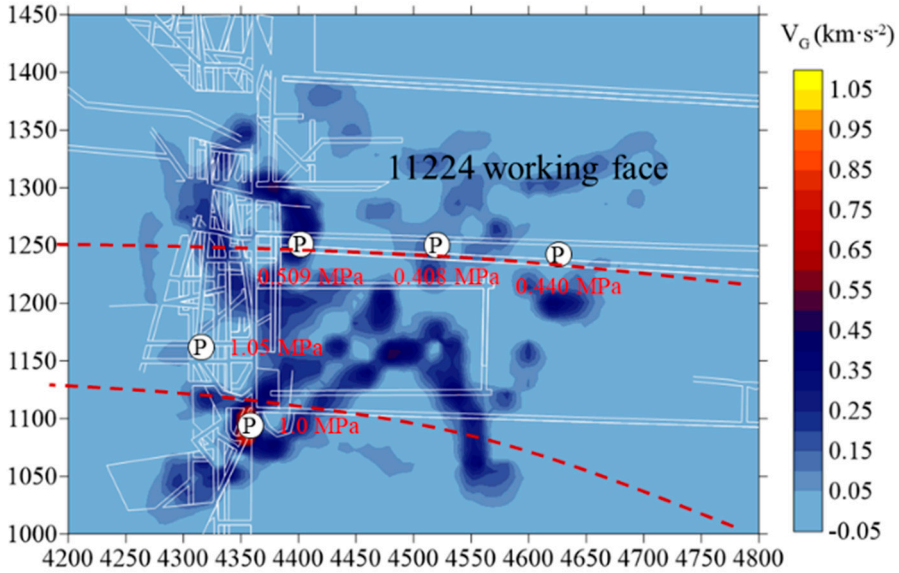

Figure 13. Revised abnormal index V_G of wave velocity gradient change.

4.2. Analysis of CT Hazardous Areas for Shock Wave in Coal Seams

The rock burst mine takes Xinzhouyao Coal Mine as its background, and the current construction location is 8308 working face in the east area of the 14-3# coal seam. There is a residual coal pillar of 11-2# coal seam above it. The 8308 working face is fully covered by probes 6, 7, 8, 11, 12, 13, 14, and 15 around it (Figure 14).

By inverting the monitoring data of the 8308 working face from 7 July 2017 to 3 August 2018, Figure 15 illustrates that the high values of the wave velocity anomaly coefficient and wave velocity gradient anomaly coefficient are located near the overlying residual coal pillar, with a wave velocity anomaly coefficient of 0.16, reaching a moderate danger level. There is a strong correspondence between the anomalously high value position and the coal pillar position, indicating that the stress and energy at the coal pillar are relatively concentrated. Figure 16 shows that during the inversion period, the working face was mined below the overlying coal pillar. Due to stress mining, the stress concentration in this area was released, causing the stress concentration zone to spread to the surrounding area. Figure 17 indicates that due to the completion of mining in the working face, the high-value areas of wave velocity and wave velocity gradient anomalies have shifted to the stop mining line position and the left and right sides of the working face at 750 m to 850 m.

Figure 14. Comparative analysis of abnormal wave velocity values.

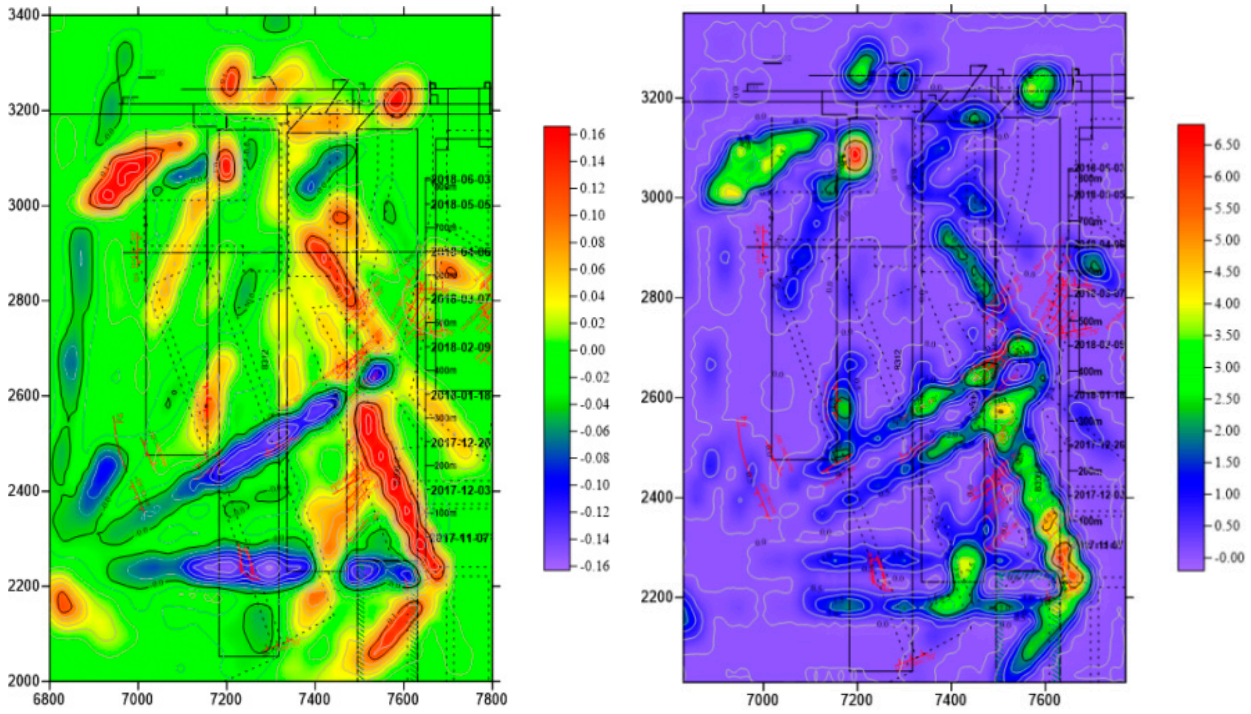

(**a**) (**b**)

Figure 15. Inversion results of abnormal wave velocity values before impact coal seam mining. (**a**) Wave velocity anomaly coefficient; (**b**) Abnormal coefficient of wave velocity gradient.

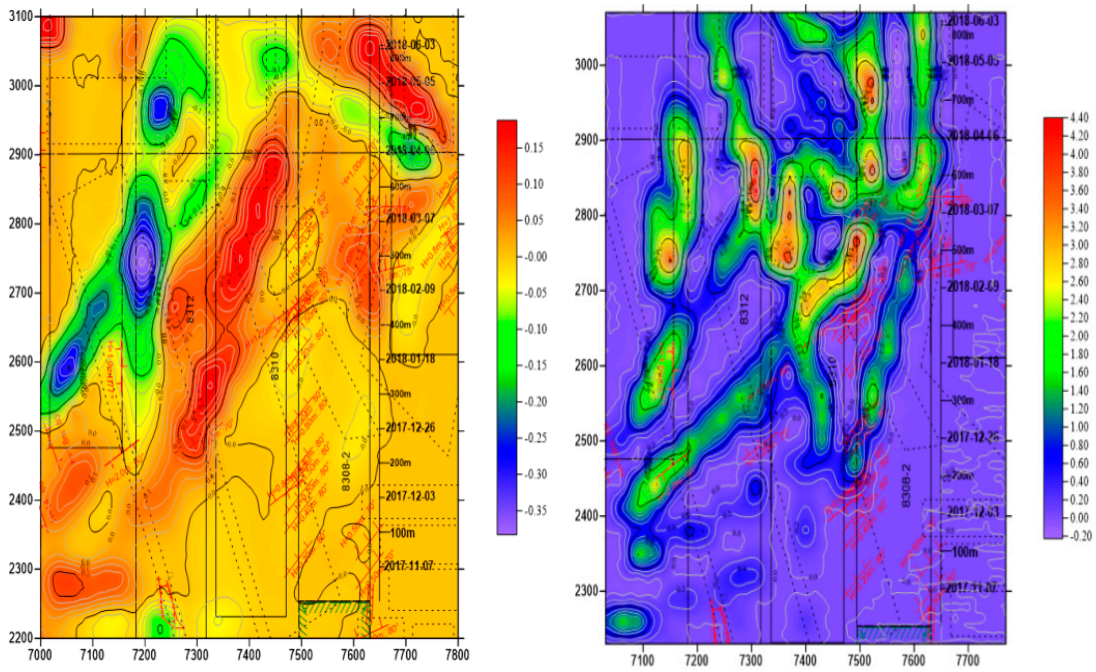

Figure 16. Inversion results of coal seam wave velocity anomaly value during mining of impacted coal seam. (**a**) Wave velocity anomaly coefficient; (**b**) Abnormal coefficient of wave velocity gradient.

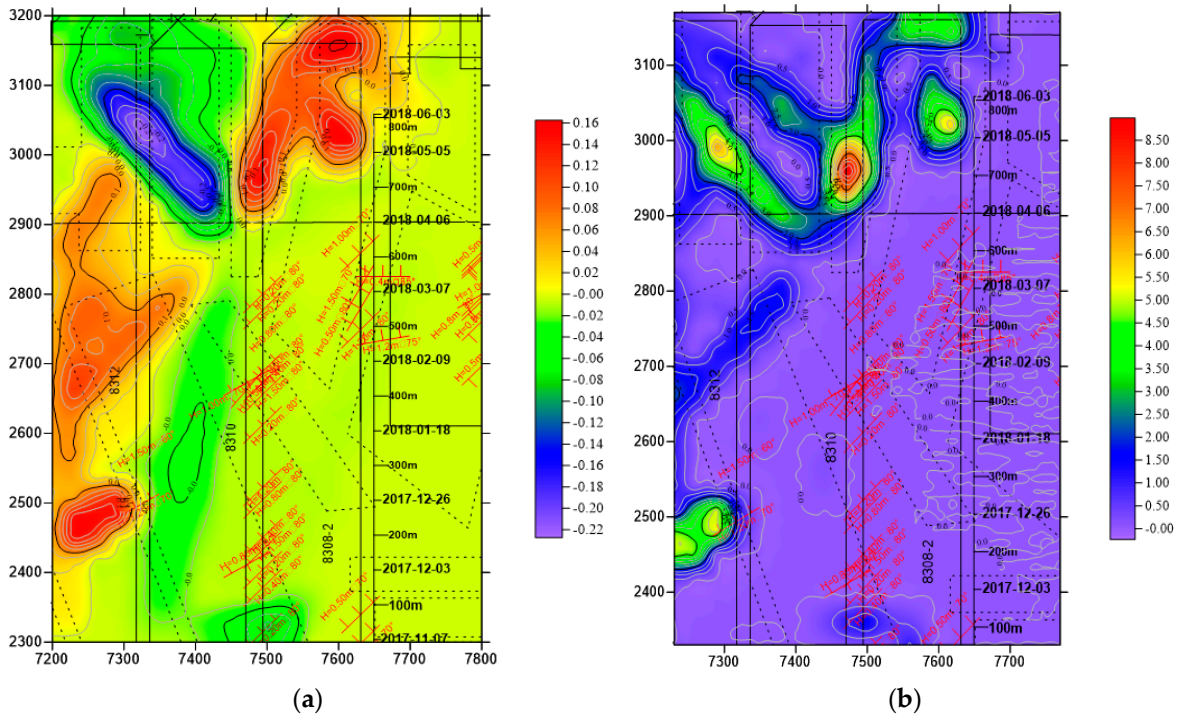

Figure 17. Inversion results of abnormal coal seam wave velocity after impact coal seam mining (after mining). (**a**) Wave velocity anomaly coefficient; (**b**) Abnormal coefficient of wave velocity gradient.

4.3. Discussion of on Site Comparison Results

Based on the results of seismic wave CT inversion, it can be observed that the high-value areas of wave velocity anomalies in outburst and impact coal seams exhibit a strong correlation with geological structures and disturbances caused by excavation. For impact coal seams, only the influence of stress on wave velocity needs to be considered,

whereas the wave velocity in outburst coal seams is jointly affected by stress and gas pressure. Experimental results indicate that the presence of gas has the effect of reducing wave velocity.

Therefore, in outburst coal seams, attention should be paid not only to high-stress areas but also to low-stress areas, as low-stress areas may be where gas accumulates. Only by adopting a comprehensive stress–gas correction method can accurate wave velocity changes be obtained. Additionally, due to uneven gas content in the coal seam, there are variations in wave velocity within the same region of the outburst coal seam. Wave velocity analysis can provide insights into the relative permeability of the coal seam.

5. Conclusions

This study investigates the disparity in wave velocity between coal burst and coal outburst phenomena using controlled laboratory experiments. It establishes a comprehensive method for characterizing stress–gas wave velocities. Subsequently, it analyzes hazardous areas in coal mines vulnerable to outburst and impact events. The primary findings are summarized as follows:

(1) The wave velocity changes between impact coal and outburst coal under load exhibit significant differences. Gas pressure negatively correlates with the wave velocity of outburst coal. Specifically, wave velocity decreases by 13.66% and 38.26% when gas pressure increases to 3 MPa and 5 MPa, respectively. In contrast, the wave velocity of impact coal shows a positive correlation with stress, increasing by 47.23% and 52% in two sets of impact coal samples as stress levels rise.

(2) To address the differences in wave velocity changes between impact coal mines and outburst coal mines, a comprehensive stress–gas coal wave velocity formula was established: $V_p = V_0 + k \cdot P_g + k_1 \cdot V_0 \cdot P_p$, improving the accuracy of wave velocity change prediction.

(3) The abnormal wave velocity coefficient ranges for outburst coal seams and impact coal seams are -0.6 to 0.25 and -0.35 to 0.16, respectively, aligning well with geological structure distribution and engineering disturbance effects. This demonstrates the accuracy of seismic CT in detecting hazardous areas.

Author Contributions: Conceptualization, Q.L., L.Q., and G.W.; methodology, Z.F.; software, Z.F. and Z.Y.; formal analysis, Z.N.; data curation, L.Q. and Y.Z.; writing—original draft, Z.F. and Q.L.; writing—review and editing, Z.C., Z.Y. and Z.N. and G.W.; visualization, Z.F. and Q.L.; funding acquisition, L.Q. All authors have read and agreed to the published version of the manuscript.

Funding: This work was supported by the State Key Research Development Program of China (2023YFC3009005), the Science and Technology Support Plan Project of Guizhou Province (No. [2023]380), and the Open Fund for Key Laboratory of Safety and High-efficiency Coal Mining, Ministry of Education (No. JYBSYS202310).

Data Availability Statement: The processed data cannot be shared at this time as the data also forms part of an ongoing study.

Conflicts of Interest: The authors declare that the research was conducted in the absence of any commercial or financial relationships that could be construed as a potential conflict of interest.

References

1. Cheng, L.; Xu, J.; Peng, S.J.; Yang, H.L.; Jiao, F.; Zhou, B.; Yan, F.Z. Dynamic behavior of outburst two-phase flow in a coal mine T-shaped roadway: The formation of impact airflow and its disaster-causing effect. *Int. J. Min. Sci. Technol.* **2023**, *33*, 1001–1017. [CrossRef]
2. Zhang, C.; Du, C.F.; Song, W.D.; Fu, J.X. Degradation effect and failure characteristics of granite under stress–seepage coupling. *Chin. J. Eng.* **2024**, *46*, 600–613.
3. Liu, J.P.; Wang, R.; Lei, G.; Si, Y.T.; Xu, S.D.; Li, Y.H. Mechanism of gas pressure action during the initial failure of coal containing gas and its application for an outburst inoculation. *Int. J. Min. Sci. Technol.* **2023**, *33*, 1511–1525.
4. Yin, S.; Li, Z.H.; Wang, E.Y.; Niu, Y.; Tian, H.; Li, X.L.; Li, H.Y.; Yang, C.J. The infrared thermal effect of coal failure with different impact types and its relationship with bursting liability. *Infrared Phys. Technol.* **2024**, *138*, 105263. [CrossRef]

5. Miao, S.J.; Shang, X.F.; Wang, H.; Liang, M.C.; Yang, P.J. Strength change mechanism of siltstone under near fatigue strength cyclic loading. *Chin. J. Eng.* **2024**, *46*, 982–993.
6. Cerrillo, C.; Jiménez, A.; Rufo, M.; Cerrillo, C.; Jiménez, A.; Rufo, M.; Paniagua, J.; Pachón, F. New contributions to granite characterization by ultrasonic testing. *Ultrasonics* **2014**, *54*, 156–167. [CrossRef]
7. Wang, X.R.; Liu, X.F.; Wang, E.Y.; Liu, S.X.; Shan, T.C.; Labuz, J.F. Microcracking characterization in tensile failure of hard coal: An experimental and numerical approach. *Rock Mech. Rock Eng.* **2024**, 1–20. [CrossRef]
8. Wang, X.R.; Wang, E.Y.; Liu, X.F. Damage characterization of concrete under multi-step loading by integrated ultrasonic and acoustic emission techniques. *Constr. Build. Mater.* **2019**, *221*, 678–690. [CrossRef]
9. He, S.Q.; Song, D.Z.; He, X.Q.; Li, Z.L.; Chen, T.; Shen, F.; Chen, J.Q.; Mitri, H. Numerical modelling of rockburst mechanism in a steeply dipping coal seam. *Bull. Eng. Geol. Environ.* **2023**, *82*, 261–284. [CrossRef]
10. He, S.Q.; Song, D.Z.; Li, Z.L.; He, X.Q.; Chen, J.Q.; Li, D.H.; Tian, X.H. Precursor of spatio-temporal evolution law of MS and AE activities for rock burst warning in steeply inclined and extremely thick coal seams under caving mining conditions. *Rock Mech. Rock Eng.* **2019**, *52*, 2415–2435. [CrossRef]
11. He, X.Q.; Liu, X.F.; Song, D.Z.; Nie, B.S. Effect of microstructure on electrical property of coal surface. *Appl. Surf. Sci.* **2019**, *483*, 713–720. [CrossRef]
12. Qiu, L.M.; Liu, Q.; Liu, Z.T.; Wang, E.Y.; He, X.Q.; Feng, J.J.; Li, B.L. Early-warning of rock burst in coal mine by low-frequency electromagnetic radiation. *Eng. Geol.* **2020**, *279*, 105755. [CrossRef]
13. Wei, M.H.; Song, D.Z.; He, X.Q.; Majid, K.; Li, Z.L.; Qiu, L.M.; Lou, Q. A three-axis antenna to measure near-field low-frequency electromagnetic radiation generated from rock fracture. *Measurement* **2021**, *173*, 108563. [CrossRef]
14. Du, L.Z.; Zhang, X.P.; Niu, J.J.; Wang, X.G.; Feng, G.L. The seismic CT method in measuring rock bodies. *Appl. Geophys.* **2006**, *3*, 192–195.
15. He, H.; Dou, L.M.; Li, X.W.; Qiao, Q.Q.; Chen, T.J.; Gong, S.Y. Active velocity tomography for assessing rock burst hazards in a kilometer deep mine. *Min. Sci. Technol.* **2011**, *21*, 673–676. [CrossRef]
16. Dou, L.M.; Cai, W.; Gong, S.Y.; Han, R.J. Dynamic risk assessment of rock burst based on the technology of seismic computed tomography detection. *J. China Coal Soc.* **2014**, *39*, 238–244.
17. Wang, Z.W.; Li, X.B.; Zhao, D.P.; Shang, X.Y.; Dong, L.J. Time-lapse seismic tomography of an underground mining zone. *Int. J. Rock Mech. Min. Sci.* **2018**, *107*, 136–149. [CrossRef]
18. Ma, X.; Westeman, E.C.; Fahrman, B.P.; Thibodeau, D. Imaging of temporal stress redistribution due to triggered seismicity at a deep nickel mine. *Geomech. Energy Environ.* **2016**, *5*, 55–64. [CrossRef]
19. Zhao, Y.J.; He, X.Q.; Song, D.Z.; Qiu, L.M.; Cheng, X.H.; Li, Z.L.; He, S.Q. Identification of the relatively low permeability area in coal and gas outburst seams by seismic wave tomography technique: Field application and validation. *J. Appl. Geophys.* **2023**, *210*, 104951. [CrossRef]
20. Khayer, K.; Shirazy, A.; Shirazi, A.; Abdolhamid, A. Permeability estimation from stoneley waves in carbonate reservoirs. *TÜRkiye Jeol. BÜLteni* **2022**, *65*, 35–42. [CrossRef]
21. Khayer, K.; Shirazy, A.; Shirazi, A.; Abdolhamid, A. Determination of archie's tortuosity factor from stoneley waves in carbonate reservoirs. *Int. J. Sci. Eng. Appl. (IJSEA)* **2021**, *10*, 107–110. [CrossRef]
22. Qiu, L.M.; Zhu, Y.; Liu, Q.; Guo, M.G.; Song, D.Z.; Wang, A.H. Response law and indicator selection of seismic wave velocity for coal seam outburst risk. *Adv. Geo-Energy Res.* **2023**, *9*, 198–210. [CrossRef]
23. Peng, Y.J.; Qiu, L.M.; Zhu, Y.; Liu, Q.; Song, D.Z.; Cheng, X.H.; Wang, C.J.; Liu, Y.J.; Sun, Q. Multi-scale multivariate detection method for the effective impact range of hydraulic fracturing in coal seam. *J. Appl. Geophys.* **2023**, *215*, 105124. [CrossRef]
24. Song, D.Z.; Liu, Q.; Qiu, L.M.; Zhang, J.G.; Majid, K.; Peng, Y.J.; Guo, M.G.; Hong, T.T. Experimental study on resistivity evolution law and precursory signals in the damage process of gas-bearing coal. *Fuel* **2024**, *362*, 130798.
25. Xue, Y.R.; Song, D.Z.; He, X.Q.; Li, Z.L.; Gong, S.Y.; Zhao, Y.J. Correlation between longitudinal wave velocity and stress in outburst coal-rock. *J. Xi'Univ. Sci. Technol.* **2019**, *39*, 826–835.
26. Zhang, B.; Wang, H.P.; Wang, P.; Li, M.T.; Yu, X.P. Macro- and microdamage characteristics and multiscale damage constitutive model of gas-bearing coal under loading. *J. Pet. Sci. Eng.* **2022**, *217*, 110848. [CrossRef]
27. Ji, S.C.; Wang, Q.; Marcotte, D.; Salisbury, M.H.; Xu, Z.Q. P wave velocities, anisotropy and hysteresis in ultrahigh-pressure metamorphic rocks as a function of confining pressure. *J. Geophys. Res.* **2007**, *112*, B09204. [CrossRef]
28. Xin, C.P.; Du, F.; Wang, K.; Xu, C.; Huang, S.G.; Shen, J.T. Damage evolution analysis and gas–solid coupling model for coal containing gas. *Geomech. Geophys. Geo-Energy Geo-Resour.* **2021**, *7*, 7. [CrossRef]
29. Wu, Y.; Wang, D.K.; Wei, J.P.; Yao, B.H.; Zhang, H.T.; Fu, J.H.; Zeng, F.C. Damage constitutive model of gas-bearing coal using industrial CT scanning technology. *J. Nat. Gas Sci. Eng.* **2022**, *101*, 104543. [CrossRef]
30. Pan, Y.S.; Wang, A.W. Disturbance response instability theory of rock bursts in coal mines and its application. *Geohazard Mech.* **2023**, *1*, 1–17. [CrossRef]
31. Shen, R.X.; Wang, X.; Li, H.; Gu, Z.J.; Liu, W. Brittleness Characteristics and Damage Evolution of Coal Under True Triaxial Loading Based on the Energy Principle. *Nat. Resour. Res.* **2024**, *33*, 421–434. [CrossRef]
32. Li, B.L.; Wang, E.Y.; Li, Z.H.; Cao, X.; Liu, X.F.; Meng, Z. Automatic recognition of effective and interference signals based on machine learning: A case study of acoustic emission and electromagnetic radiation. *Int. J. Rock Mech. Min. Sci.* **2023**, *170*, 105505. [CrossRef]

33. Cao, A.Y.; Wang, C.B.; Dou, L.M.; Li, Y. Dynamic manifestation mechanism of mining on the island coalface along fault and dynamic pre-warning of seismic waves with seismic tomography. *J. Min. Saf. Eng.* **2017**, *34*, 411–417.
34. Shen, R.X.; Hou, Z.H.; Yuan, Z.C.; Li, Y.W.; Gu, Y. Development of a Three-dimensional Stress Monitoring System for Coal Rock and its Application in a Mine. *Rock Mech. Rock Eng.* **2024**, *57*, 1983–1996. [CrossRef]